SLAC-TN-04-065
September 2004

Simulation of Transmission and Attenuation of Photons in a Labyrinth

Kai M. Hudek
Colorado School of Mines, Golden
Stanford Linear Accelerator Center
Menlo Park, CA
July 19, 2004

Work supported in part by Department of Energy contract DE-AC02-76SF00515.

Table of Contents

Table of Figures

Abstract

Simulation of Transmission and Attenuation of Photons in a Labyrinth. KAI M. HUDEK (Colorado School of Mines, Golden, CO 80401). ALBERTO FASSO (Stanford Linear Accelerator Center, Menlo Park, CA 94025). HEINZ VINCKE (Stanford Linear Accelerator Center, Menlo Park, CA 94025).

Neutrons travel through tunnels and ducts (labyrinths) according to curves that are universally applicable, regardless of labyrinth geometry or particle energy. Photons were believed to follow this manner, but this has been found not to be the case. Photons transmit through labyrinths with a definite functional dependence upon both particle energy and labyrinth geometry. In the first leg of a two-legged labyrinth, photons attenuate according to the function

$$Dose = \frac{1}{1 + A \cdot x^2}$$

In the second leg, photons attenuate according to the function

$$Dose = \frac{1}{1 + B \cdot x^3}$$

in which A and B are functions of energy and labyrinth geometry, and x is a dimensionless unit of d/sqrt(a) in which d is the distance from the labyrinth mouth and a is the cross-sectional area. Dose is an attenuation factor. The A and B values have not been analyzed sufficiently to determine their functional dependence upon energy and cross-sectional area, however they have been tabularized which allows for interpolation of the data for use in calculations.

These results were determined by simulating a mono-energetic beam incident upon a two-legged labyrinth with angular spread to cover the mouth. Work was begun on utilizing a real spectrum to determine a functional dependence by placing an iron target at the mouth of the labyrinth, and striking it with an electron beam. However, the

techniques used to gather the mono-energetic beam data were not sufficient to effectively gather a complete set of real spectrum data and analyze its functionality.

Introduction

Emission of photon radiation, particularly γ-rays and x-rays, from an electron accelerator poses a major threat to personnel if above a certain level. Thus, the design of biological radiation shielding is of great importance. The weakest sections of the shield are the ducts and tunnels (labyrinths), which act as leakage paths for radiation. A generalized labyrinth is shown in Figure 1[1]. Low energy neutrons, which are a primary byproduct of proton accelerators and a secondary byproduct of electron accelerators, are transmitted through labyrinths according to the universal transmission curves shown in Figure 2. Transmission in the first leg should follow one of three curves (Figure 3) [2], depending upon incident beam type; this project utilizes an isotropic point source [4]. The second and subsequent legs follow the same universal transmission curve (Figure 4) [3]. It is expected that photons (of energy ranges 100 KeV to 1 GeV) which are copiously produced by electron accelerators and synchrotrons, but not proton accelerators, will follow similar, though still universal, transmission curves. The project propounds to use FLUKA (a Monte Carlo type simulation package) to simulate the streaming of photons through the two-legged labyrinth shown in Figure 5. The goal is to recreate the universal neutron transmission curves for photons, therefore increasing the accuracy and efficiency of calculations based upon these curves.

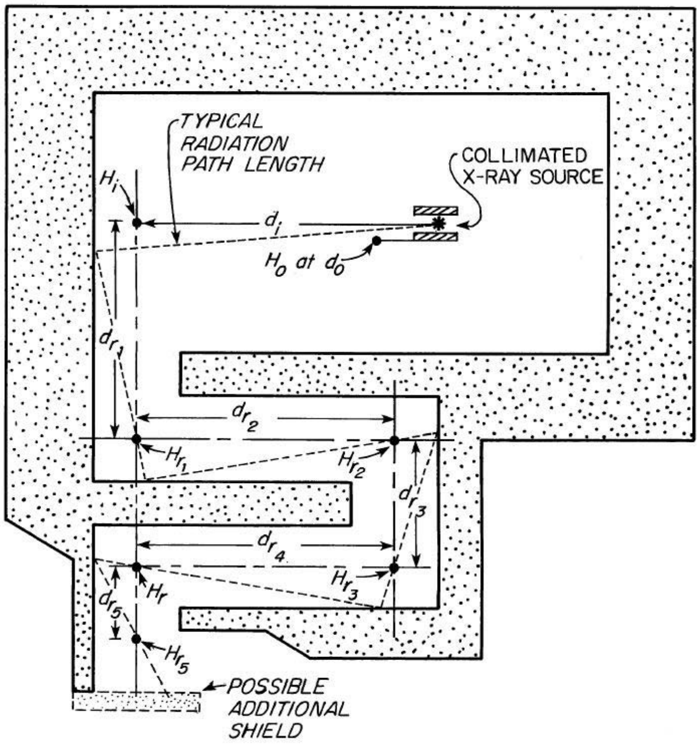

Figure 1: Generalized labyrinth design showing successive reflections of photons through the labyrinth and approximated by centerline distances. For latter simulations, the collimated x-ray source was replaced by an electron beam incident on an iron target.

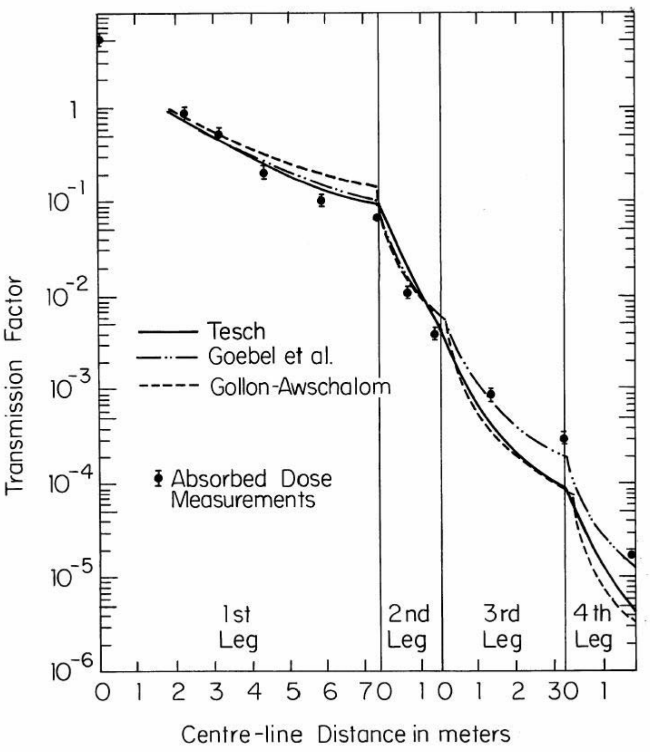

Figure 2: Absolute transmission through a labyrinth.

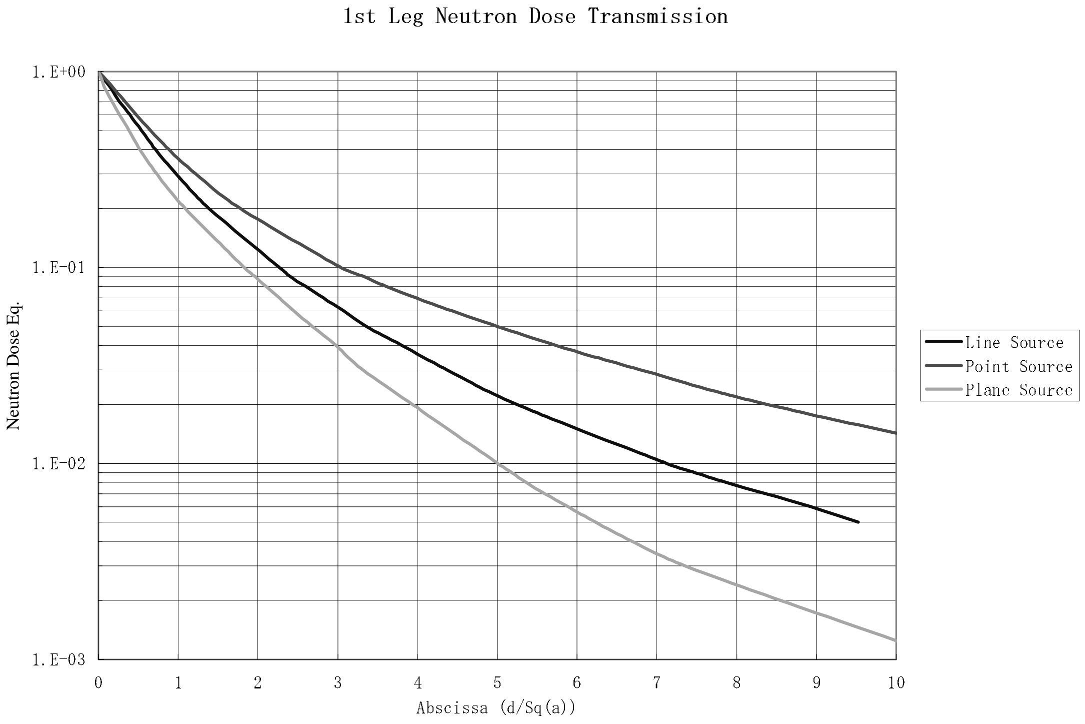

Figure 3: Universal transmission curves for the first leg of a labyrinth.

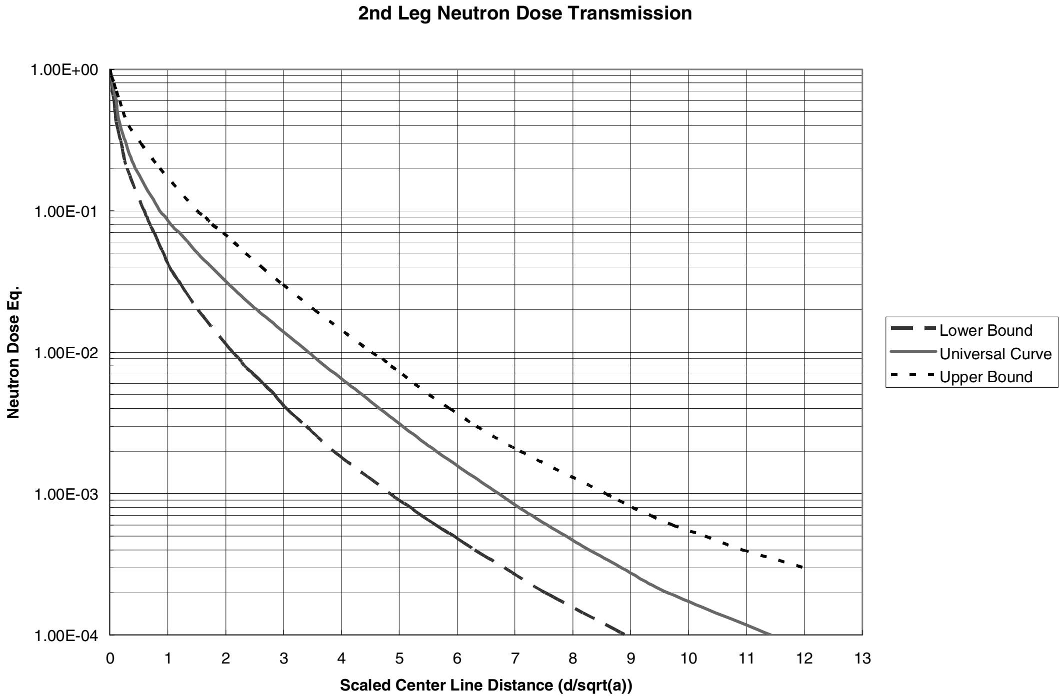

Figure 4: Universal transmission curves for 2nd and subsequent legs of labyrinths. The bounds represent confidence levels.

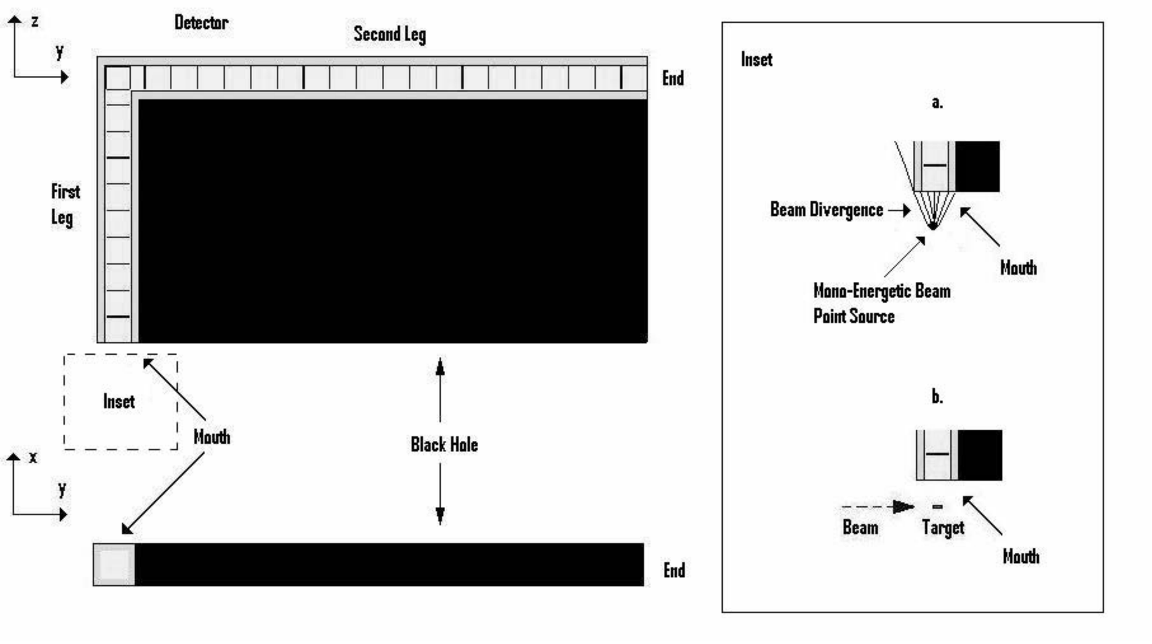

Figure 5: Project specific labyrinth. Yellow is air, grey is concrete, the large black rectangle is 'black hole,' the black tick marks are detectors, white is vacuum, and the target is iron. Inset: a. the mono-energetic beam incident on the mouth of the labyrinth; b. the iron target simulation.

Methodology

Gathering and processing data from FLUKA comprises a significant part of this project. The geometric dimensions shown in Figure 5 were created as parameters in which to run the FLUKA simulations. To test the transmission as a function of geometry, the mouth and the depth of the labyrinth were scaled proportionately so that the first leg stayed approximately 10, in scaled units of $d/\sqrt{a}$ in which d is the distance into the tunnel as measured from the mouth and a is the cross-sectional area of the tunnel, excluding the width of the concrete walls. The second leg stayed approximately $20d/\sqrt{a}$. To test the transmission as a function of energy, each geometry was fed a mono-energetic beam of photons aimed at the mouth of the labyrinth, with a beam divergence enough to cover the width of the opening. Detectors were scored along the legs at regular intervals of approximately $1\,d/\sqrt{a}$. FLUKA runs were then submitted parallel to the batch [server] with the maximum sustainable particle number (constrained by the batch [server] execution time limit) in order to return the cleanest statistics with little error. The response gathered from the data was renormalized to 1 at the beginning of each leg to obtain the net attenuation factor, independent of the incident particle flux.

Data was taken at five energies: 100 KeV, 1 MeV, 10 MeV, 100 MeV and 1 GeV for five different geometries. The cross-section of the tunnel was kept square for all runs and data taken for a side length equal to 50 cm, 100 cm, 200 cm, 300 cm and 400 cm. In all, 25 distinct simulations were preformed. Analysis of the data shoes that that the photon transmission simulated by FLUKA did not agree with the prediction of a universal transmission curve.

Because the mono-energetic beam simulations were simplified and unrealistic, a more substantial situation was employed in order to observe the results. An iron cylinder with a radius of 2” (5.08 cm) and length of 12” (30.48 cm) was used as a fixed target for an accelerator collision. Incident upon it was a 1 GeV mono-energetic beam of electrons directed and centered along the cylinder axis, perpendicular to the plane of the labyrinth mouth. The resulting transmission of random photons and other particles was then scored to determine if the geometric and energetic dependencies would average themselves out.

The largest obstacle in the iron target collision simulations is achieving clear statistics. Only a small fraction of the particles produced in the collision find a path into the labyrinth (**Error! Reference source not found.**). This causes CPU loss tracking particles through the vacuum which are of no interest to the simulation. Submitting jobs to the batch [server] queue is less useful because it can handle only a very small number of particles. Therefore, computer rp-group1 (P4 3.2GHz) was incorporated to handle the more time consuming simulations.

A deep first leg leads to a lower photon transmission within the second leg. To increase the clarity of the statistics in the second leg, the first leg was shortened to $5\,d/\sqrt{a}$. Also, the FLUKA input file was modified to utilize the symmetry of the particle shower emanating from the iron target/electron beam collision; the particle shower is isotropic with respect to rotation around the beam axis. An identical copy of the labyrinth was scored opposite to the original with +/-Z symmetry in order to capture a greater portion of the particle shower produced in the collision. Detectors in both regions were redefined as a single region, effectively doubling the photon flux.

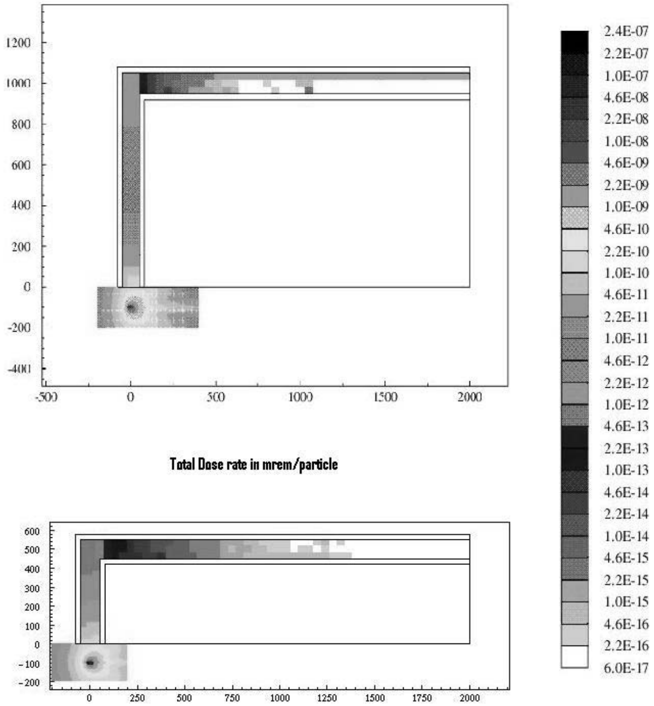

Figure 6: Total dose rate in mrem/particle showing a first leg of $10\,{}^{d}\!/\!{}_{\sqrt{a}}$ (top), and a first leg of $5\,{}^{d}\!/\!{}_{\sqrt{a}}$ (bottom). NB: large portion of particles produced in iron target collisions are transferred forward and do not interact with the system.

Assumptions

A constant 30 cm concrete layer surrounded the labyrinth. The detectors were scored to cover the entire mouth area, apart from a constant 5 cm band near the walls; this reduces the effects of back scattering from the walls. The detectors were kept a constant 1 cm thick. The mono-energetic beam was kept a scaled distance, equal to the dimension of the labyrinth (length of a side sans concrete), from the mouth of the labyrinth in order to maintain a constant beam divergence. The iron target was maintained a distance of 1 m from the mouth centerline, regardless of labyrinth dimension in order to increase particle flux into the labyrinth. A 1 GeV electron beam was used in all iron target simulations to mimic an electron accelerator beam and to produce the maximum number of particles from the resultant collision. The area outside the labyrinth was kept in vacuum, while the space inside the labyrinth was filled with air. A ‘black hole’ was situated in the bend of the labyrinth (Figure 5) to stop extraneous particles from entering the second leg.

FLUKA

FLUKA reads its input from two files: an input file and a PEMF file. Mono-energetic beam input files include a geometry definition, region definition, material definition, color plot detector scoring and photon detector scoring. Iron target collision input files include all of the above; in addition there is the need to modify the original labyrinth geometry, a new target geometry, region definition, addition of an electron beam, additional detector scoring for neutrons and total dose, additional color plot detector scoring and a second labyrinth, identical to the original. Mono-energetic beam PEMF files include an 'AIR' compound definition and a 'CONCRETE' compound definition. Iron target collision PEMF file includes an 'IRON' material definition in addition to the other two.

Certain biasing techniques are applied to increase the clarity of the statistics while decreasing CPU time. EMF-BIAS activates leading particle bias; therefore in an EM shower, FLUKA will track the highest energy particle produced and weight it accordingly. PHOTONUC activates high-energy photon-nucleus interactions.

Once a FLUKA run has terminated, all detector responses are extracted and plotted using Microsoft Excel™. Graphs are grouped by energy and also geometry.

Color plot detectors responsive to particle flux are scored in a Cartesian mesh around the target, the first and second leg, not including the concrete, and converted into mrem using conversion factors. Mrem/electron scoring is then displayed via color plots. Color plots are used primarily to visually gauge the statistics of a given run.

Results

The simulations were broken up into two categories: the mono-energetic beam and the real target. For simplicity and to gain a better understanding, the initial FLUKA simulations were fed a mono-energetic beam of photons in the methods described previously. Once aberrations were seen from the expected energetic and geometric independence, an iron target was placed at the mouth and struck with a mono-energetic beam of electrons to create a different spectrum of photons with diverse energies. The iron target collision runs, however, showed similar dependencies as seen in the mono-energetic beam simulations. Upon this realization, the data was then fit to a simple functional form that would be useful for making radiation safety calculations.

Mono-Energetic Beam

The first leg transmission shows itself to be a function of energy and geometry. The original prediction states the opposite. Figures 7, 8 and 9 illustrate the photon transmission's functional dependence on geometry. Figures 10 and 11 illustrate the photon transmission's functional dependence on energy.

At higher energies, the first leg geometric dependence is near zero (Figure 7). At lower energies, the first leg geometric dependence can be clearly seen; the 50 x 50 cm labyrinth has approximately 2 times greater flux at 10 $d/\sqrt{a}$ than the 400 x 400 cm labyrinth (Figure 9). Transmission seems to have a weighted dependence on the area other than a strict $d/\sqrt{a}$, otherwise the curves of different geometry would overlap at the same values in the units of $d/\sqrt{a}$. Instead, a larger cross-section of area for the mouth leads to a higher attenuation, as stated above.

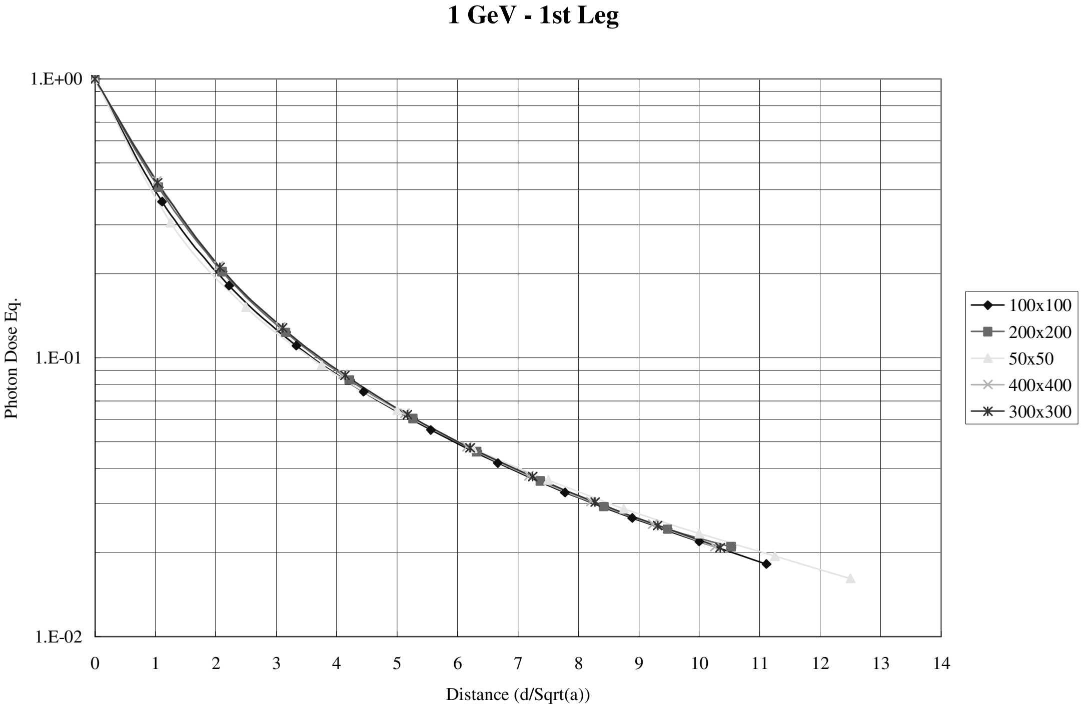

Figure 7: Highest energy's first leg transmission showing no geometry dependence.

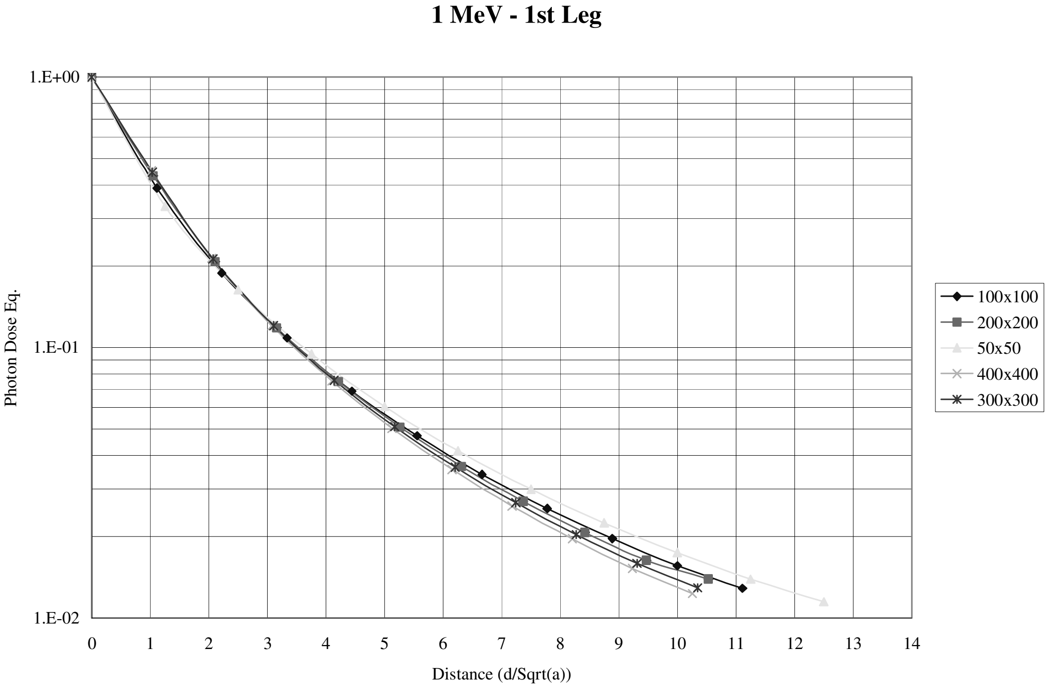

Figure 8: Mid-level energy first leg transmission showing some geometry dependence.

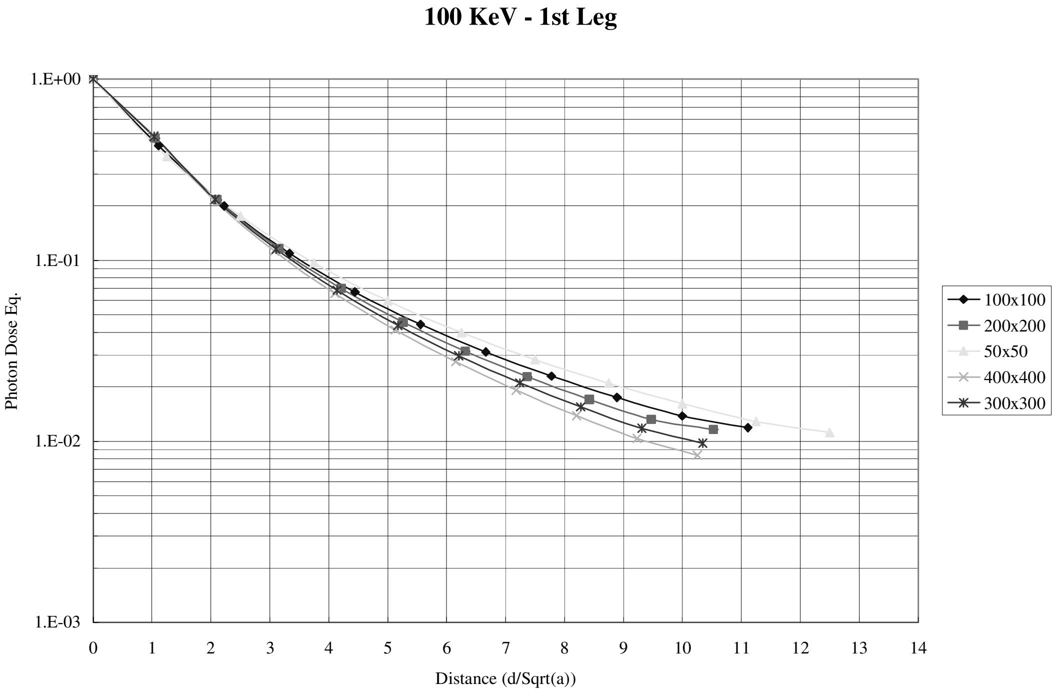

Figure 9: Lowest energy run’s first leg transmission showing definite geometry dependence.

The first leg energetic dependence follows a pattern (shown in Figures 10 and 11) in which the highest energy has the least attenuation and the lowest energy has the greatest. The difference in transmission can be as much as 2.5 times in the 400 x 400 cm labyrinth (Figure 10).

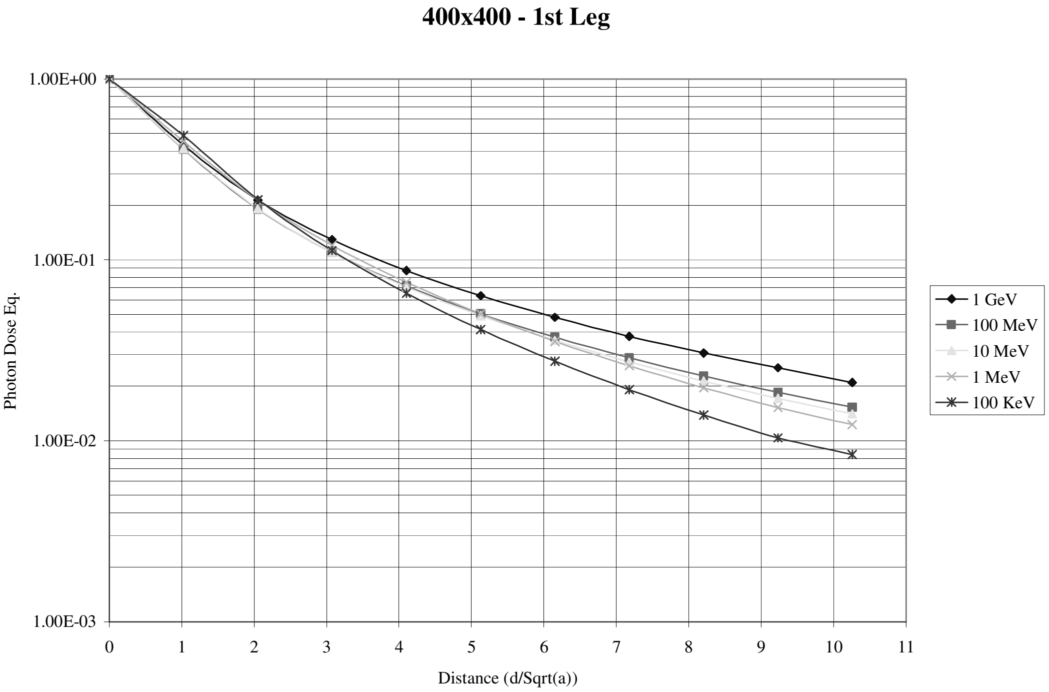

Figure 10: First leg transmission curves for a square, 400 by 400 cm labyrinth showing energy dependence.

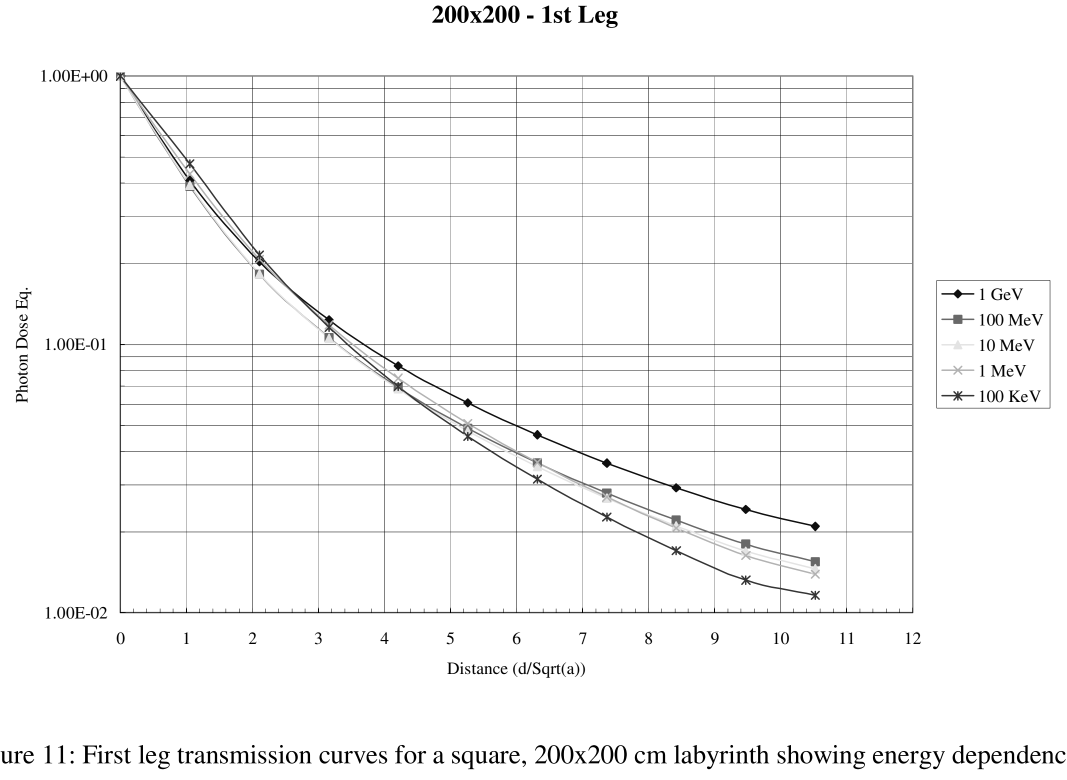

Figure 11: First leg transmission curves for a square, 200x200 cm labyrinth showing energy dependence.

Second leg data also shows a functional dependence on both energy (Figure 12) and geometry (Figure 13). The energetic dependence diverges by nearly a factor of 10 at only 1 $d/\sqrt{a}$ from the beginning of the second leg (Figure 12, 100 KeV vs. 100 MeV), whereas the geometric dependence never diverges quite so severely (Figure 13). The reliability of the statistics weakens farther down the leg, which is to be expected from the low particle flux. Therefore, accurate analysis of this region is more difficult; however, most of the poor statistics in the photon dose occur where there is minimal attenuation with increased distance, a region of little interest to the design of shielding. Also, a depth of this magnitude is never applied in practice. Even 10 $d/\sqrt{a}$ is long, but 20 $d/\sqrt{a}$ was attempted for educational purposes.

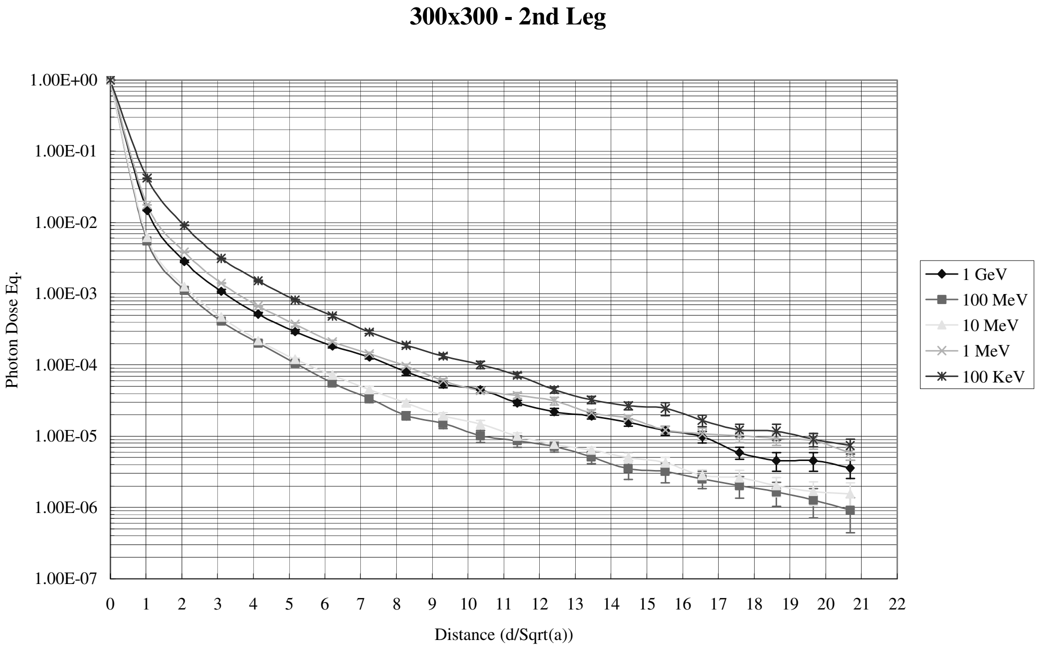

Figure 12: Second leg transmission showing energy dependence.

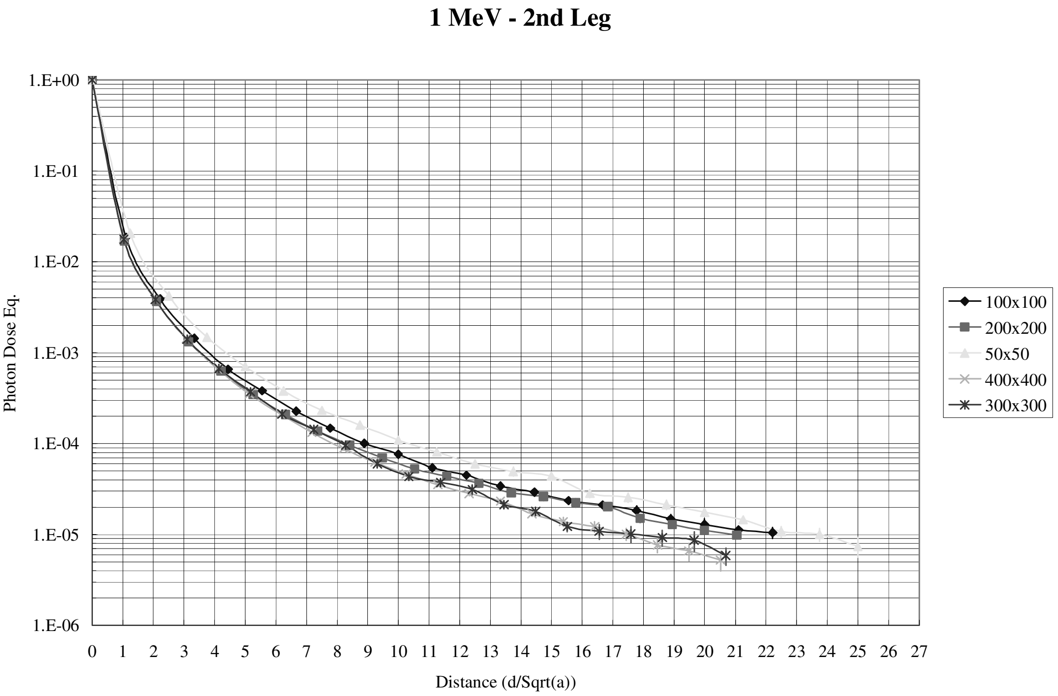

Figure 13: Second leg transmission showing geometry dependence.

Iron Target Collision

Figure 14 shows that as the distance traveled down the second leg increases, the total flux decreases dramatically until individual particle tracks can be seen. White represents zero energy deposition; i.e. zero particle flux. Total dose and neutron dose were also scored in addition to the photon dose for the iron target collision runs, as shown in Figures 14 and 15.

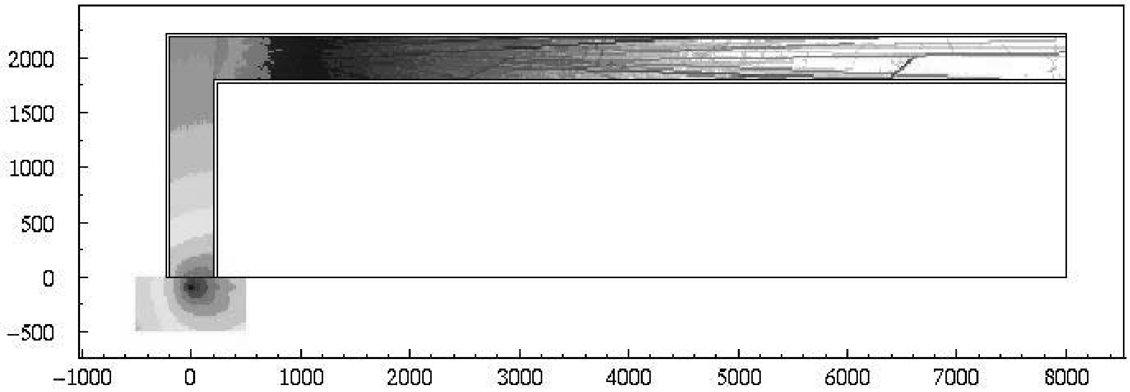

Figure 14 - Color plot showing particle plume (lower left) and low statistics at the end of the second leg. The long streaks are individual particle tracks. No data was taken from this run; the plot is only for effect.

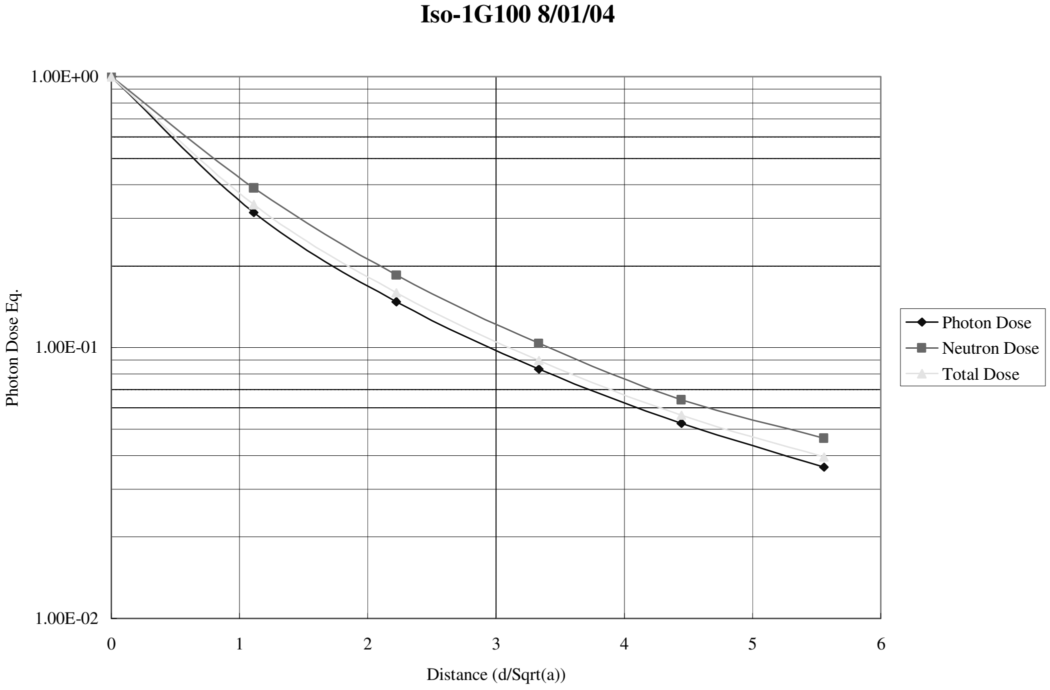

Figure 14: First leg iron target transmission data for 1 GeV beam energy.

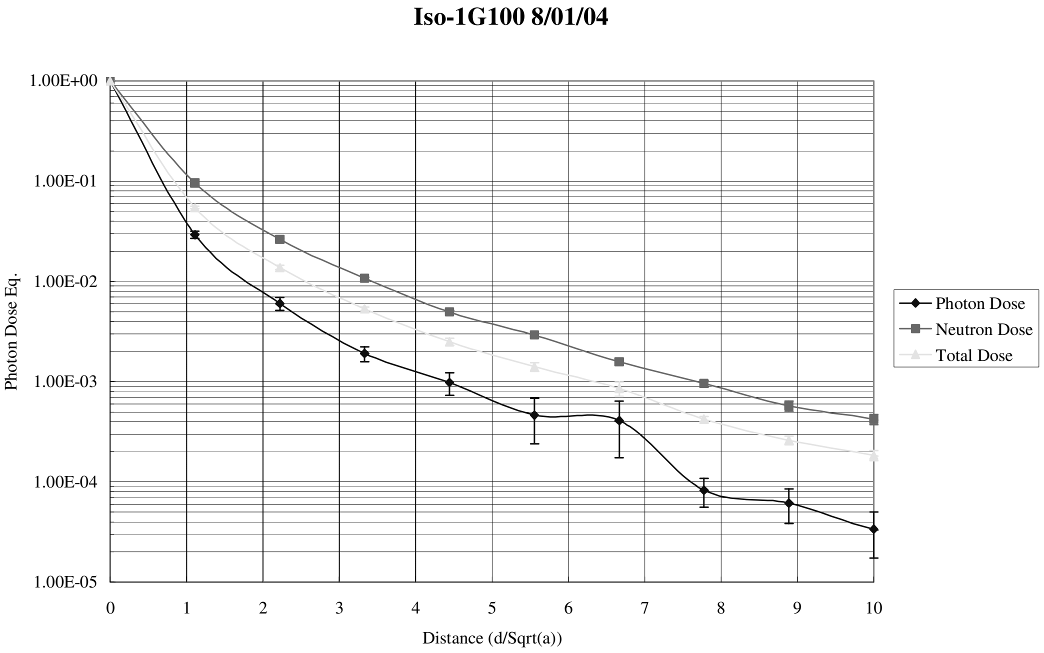

Figure 15: Second leg iron target transmission data for 1 GeV beam energy.

The first leg for the iron target collision runs show, more markedly than the mono-energetic beam runs, a geometric dependence with a constant energy (Figure 15). Whether or not there is an energetic dependence is yet unknown because no successful trials of energy other than 1 GeV have been run. The statistics weaken greatly as the beam decreases in energy. Not as many particles are generated by the iron target/electron beam collision thus leading to a lower particle flux entering the labyrinth. After 5 runs, the total response of the detectors for the 100 KeV and 1 MeV runs read all zeros, and for the 10 MeV and 100 MeV runs mostly zeros. It can be inferred from the mono-energetic data that there will be a functional dependence upon energy. The second leg statistics are too weak to draw any valid conclusions (Figure 16). In regions where the curves are not smooth, or have error bars that span an order of magnitude, are due to statistical fluctuations an can be thrown out.

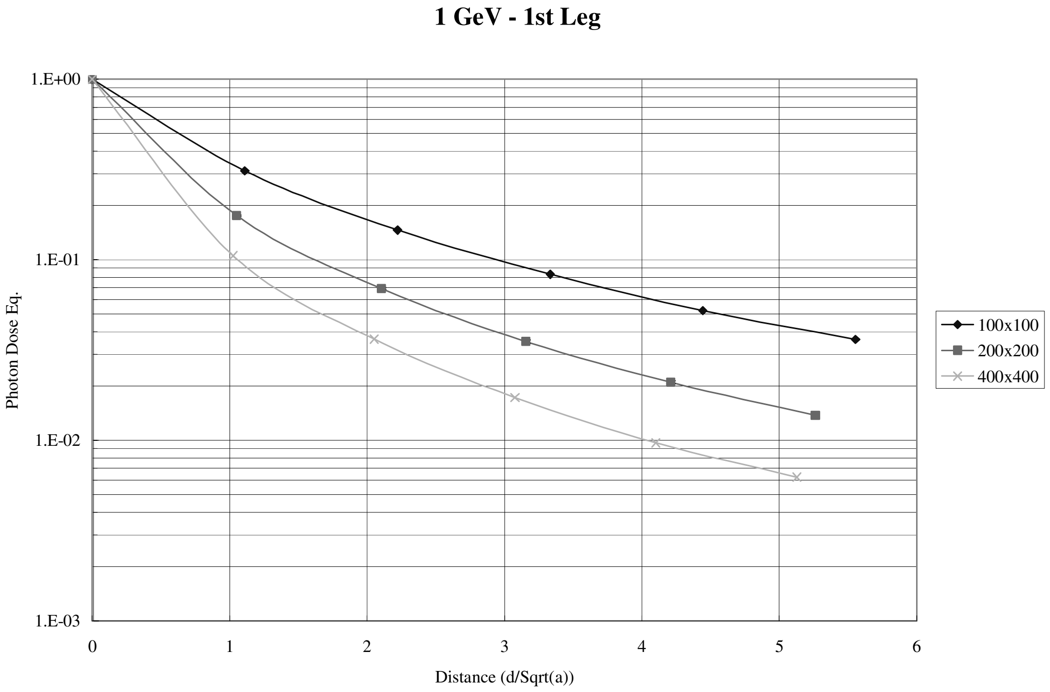

Figure 16: First leg iron target collision transmission showing a geometric dependence.

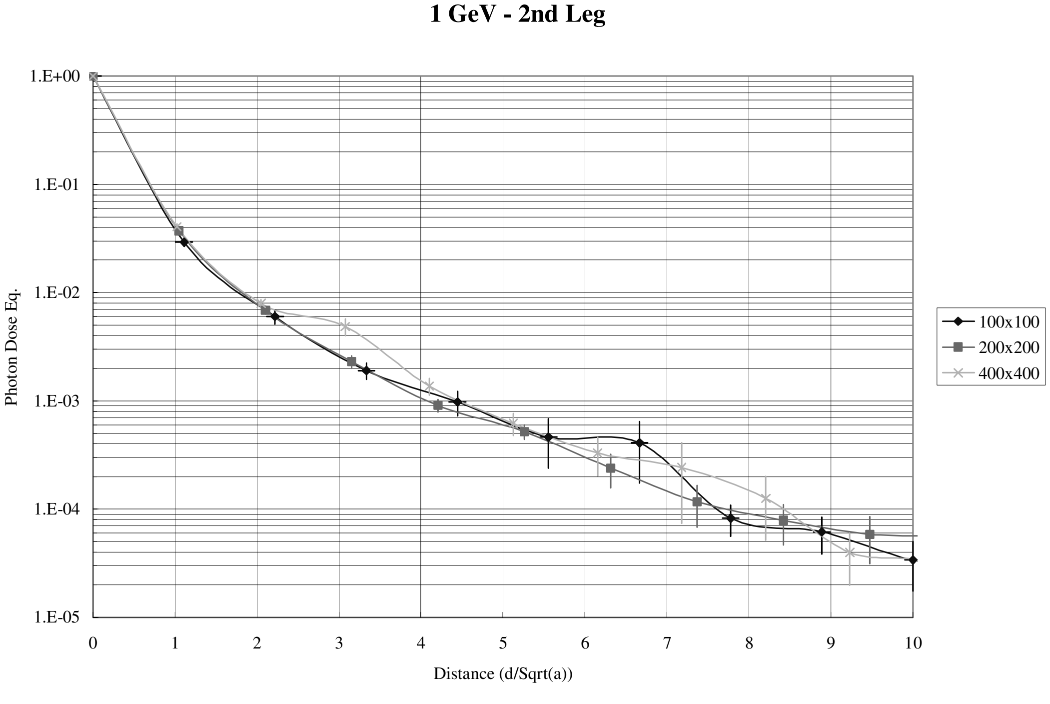

Figure 17: Second leg iron target collision transmission. Caveat: those points where the error bars span an order of magnitude or more can be disregarded.

The data accumulated thus far for the iron target simulations do not suggest that the photon transmission's functional dependence on energy and geometry are specific to the simplified mono-energetic beam simulations.

Comparison Techniques

The results from both the mono-energetic beam and the iron target runs are compared to previous experimentation and calculation. The first leg is plotted next to a geometric $1/r^2$, the point source curve from Figure 3, and Equation 1 [5],

$$H = 2.12(1.5 + d)^{-1.85} \tag{1}$$

in which H is the measured dose and d is the same as previously stated. Mono-energetic runs are shown in Figures 18, 19 and 20; iron beam target runs are shown in Figure 19. The $1/r^2$ curve was calculated using Equation 2,

$$Dose_n = Dose_0 \left(\frac{x_0}{x_n} \right)^2 \tag{2}$$

in which $Dose_n$ is the photon dose equivalent at detector n, x_n is the distance (in $d/\sqrt{a}$) from the source to detector n, $Dose_0$ is the photon dose equivalent at the mouth of the labyrinth (normalized to 1), and x_0 is the distance (in $d/\sqrt{a}$) from source to mouth.

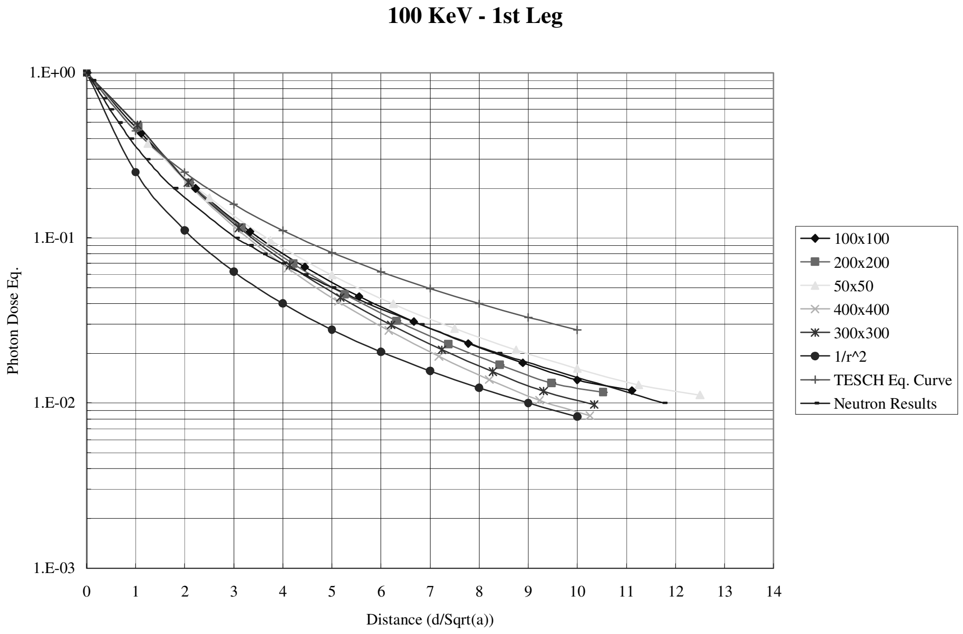

Figure 19 - First leg curve for low energy with previous results.

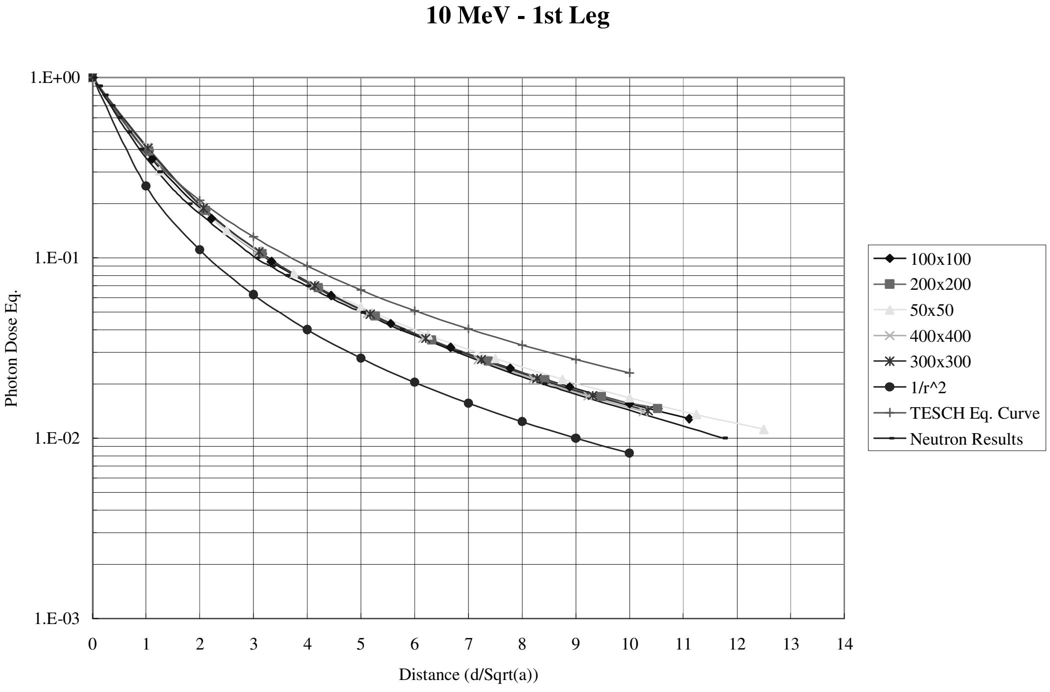

Figure 18: First leg curve for mid-level energy with previous results.

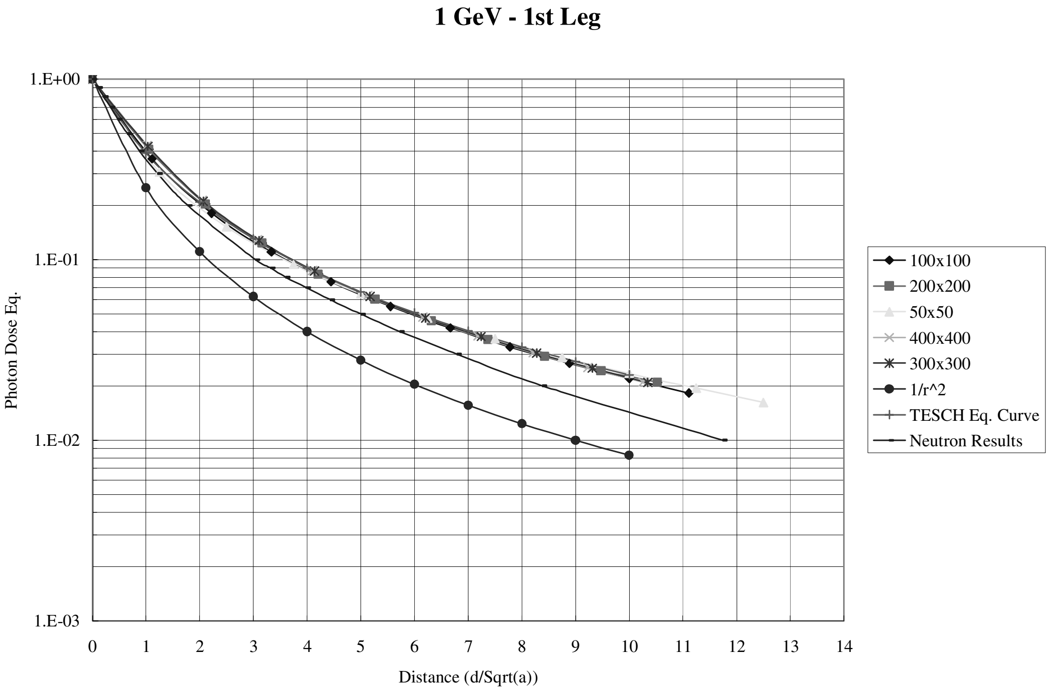

Figure 19: First leg curve for high energy with previous results.

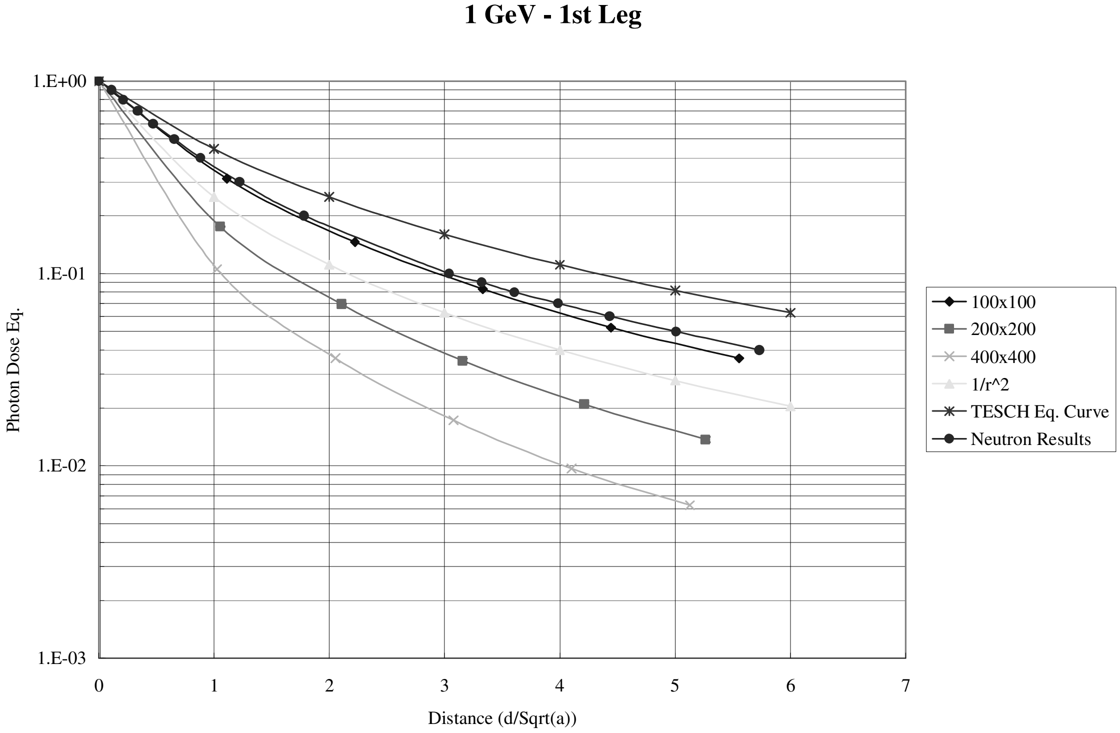

Figure 20: First leg curve for iron target collision with previous results.

The second leg transmission for the mono-energetic beam was compared with the neutron transmission in Figure 4 (Figure 20). The second leg transmission for the iron target collision was also compared with the neutron transmission in Figure 4 (Figure 23). The photon transmission follows approximately the lower bound of the transmission curve.

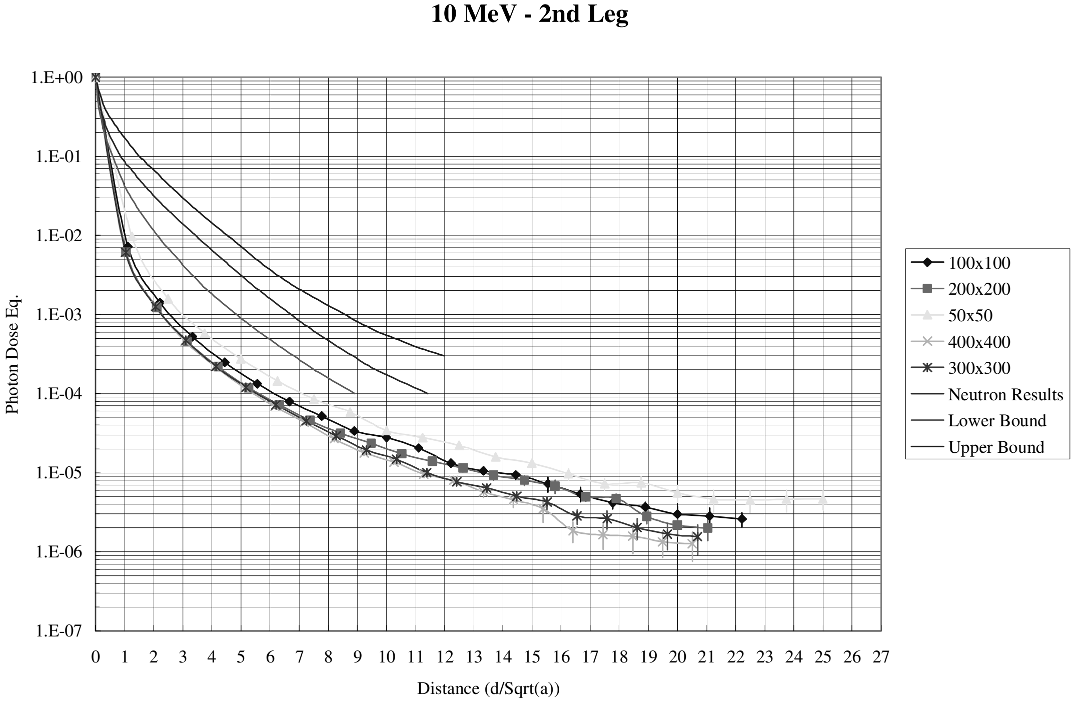

Figure 21: 10 MeV second leg mono-energetic source with universal curve and confidence bounds.

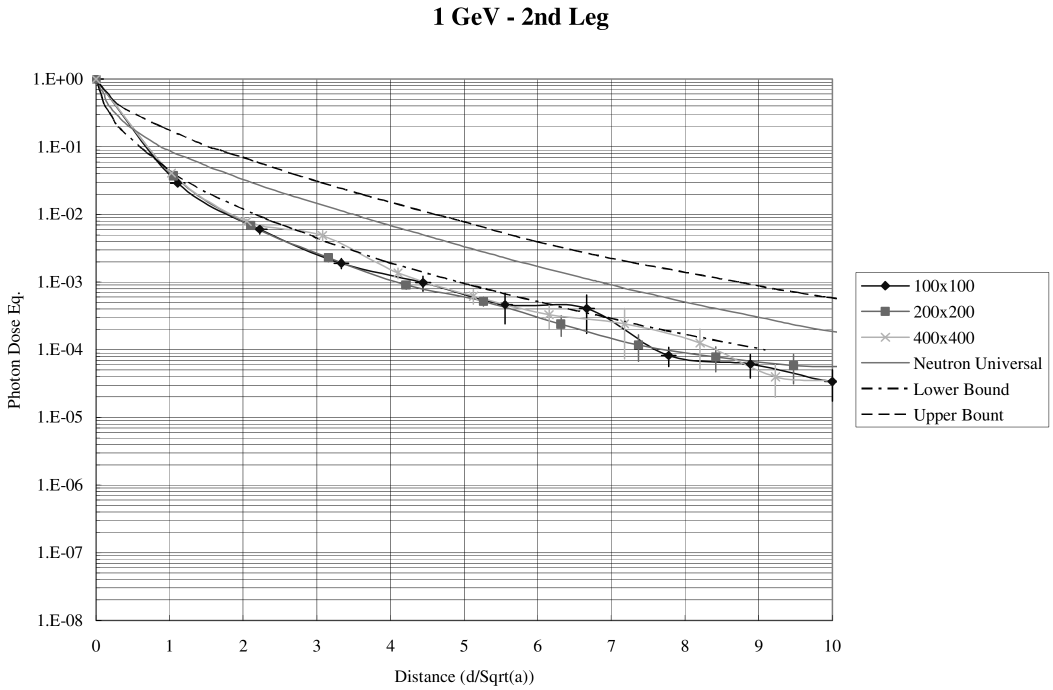

Figure 22: 1 GeV second leg iron target collision curve with universal curve and confidence bounds.

The results from the iron target runs differ greatly from the mono-energetic beam runs in the first leg (Figure 25). The radiation from the real target collision attenuates to a factor of 5 times less (at around 5 $d/\sqrt{a}$) than the mono-energetic beam's first leg. A possible explanation for this is that a large number of particles are incident on the first detector in the iron target runs, but are traveling in a direction that is near enough to parallel with the mouth that many are back scattered or transmit through the concrete into the 'black hole' (Figure 5); thus fewer pass down the labyrinth. This changes the angular distribution of the incident particles and changes how they "see" the first leg. Instead of their primary transmission being due to the scattering off of the back wall of the first leg, they now get scattered at least twice.

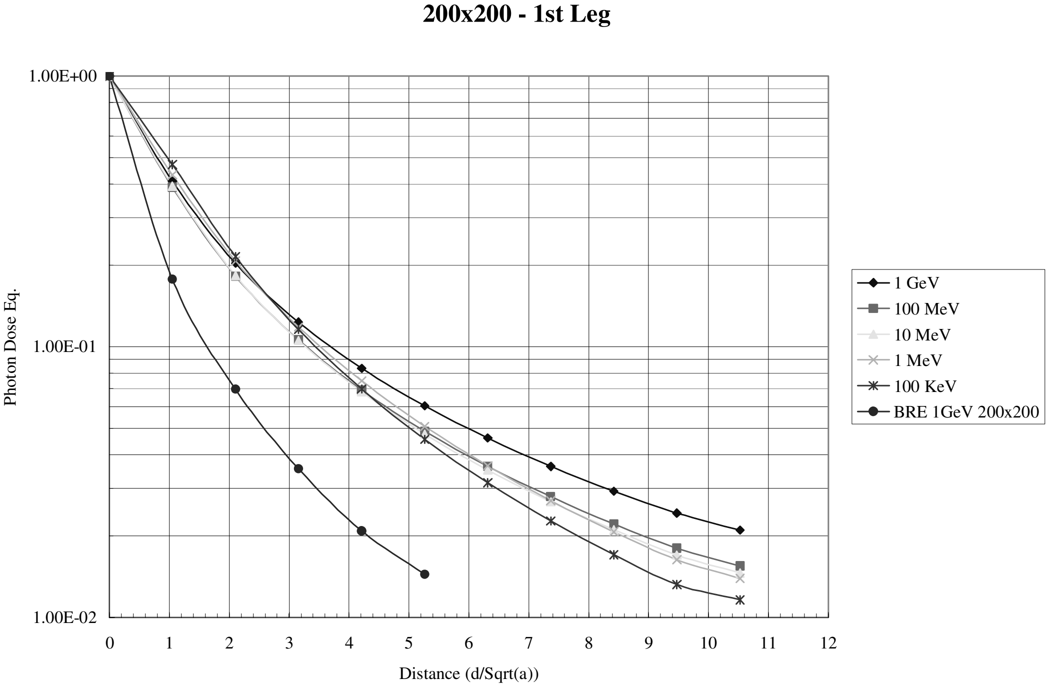

Figure 23 – First leg iron target collision curve for the 200 x 200 cm labyrinth compared to the mono-energetic beam curves also 200 x 200 cm.

As expected, the transmission curve for the second leg of the iron target collision falls within the bounds of the mono-energetic transmission curves (Figure 26). The energy distribution of the particles at the end of the first leg is somewhere in between the energy ranges and it has approximately the same angular distribution as

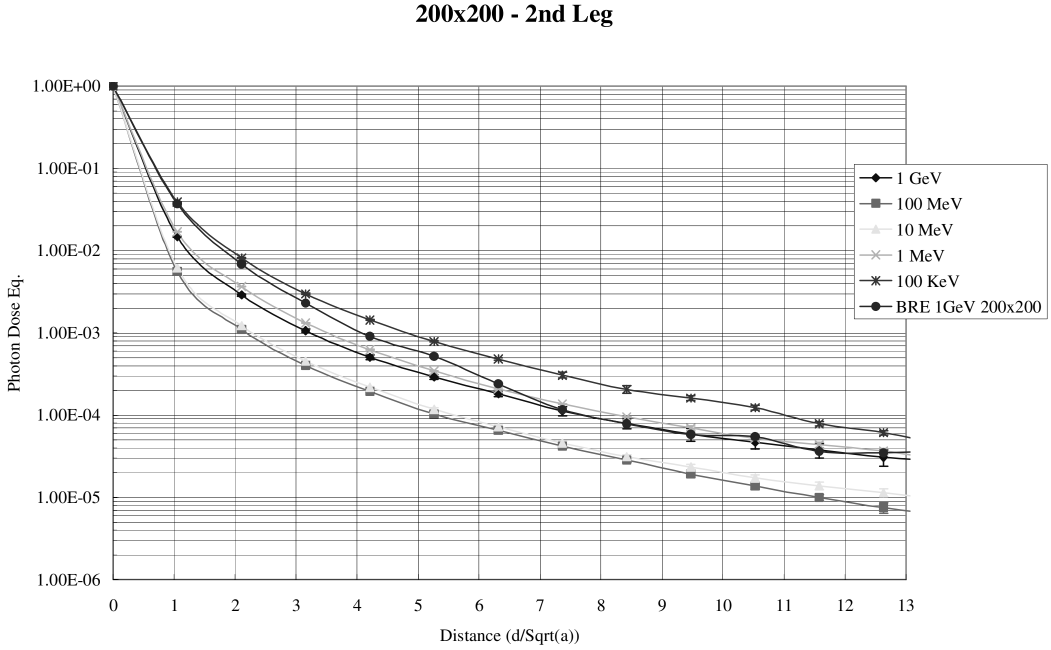

Figure 24 – Second leg iron target collision curve for the 200 x 200 cm labyrinth compared to the mono-energetic beam curves also 200 x 200 cm.

Mono-Energetic Beam - Functional Fitting

The iron target simulations and the mono-energetic beam simulations show a similar functional dependence on energy and geometry.

It is apparent that none of the three curves plotted against data in the previous section are satisfactory in describing the transmission of photons because the data has a functional dependence on both energy and geometry. Although both the iron target and the mono-energetic beam simulations showed this functional dependence, the mono-energetic beam has a more complete set of data with which to analyze. The following analyses were are completed using the mono-energetic beam data.

The photon transmission was thought to have the form of Equation 3,

$$Dose = \frac{1}{1 + C(E,a)x^n} \tag{3}$$

in which C is constant dependent upon energy and cross-sectional area, and x equals $d/\sqrt{a}$.

Rearranging Equation 3 to solve for *C(E,a)* and *n* results in Equation 4, which is plotted in Figures 27 and 28.

$$C(E,a)x^n = y - 1 \tag{4}$$

in which *y* equals *1/Dose*. *C(E,a)* will have two values: *A(E,a)* for the first leg and *B(E,a)* for the second leg. *n* will also have two values, one for both *A(E,a)* and *B(E,a)*.

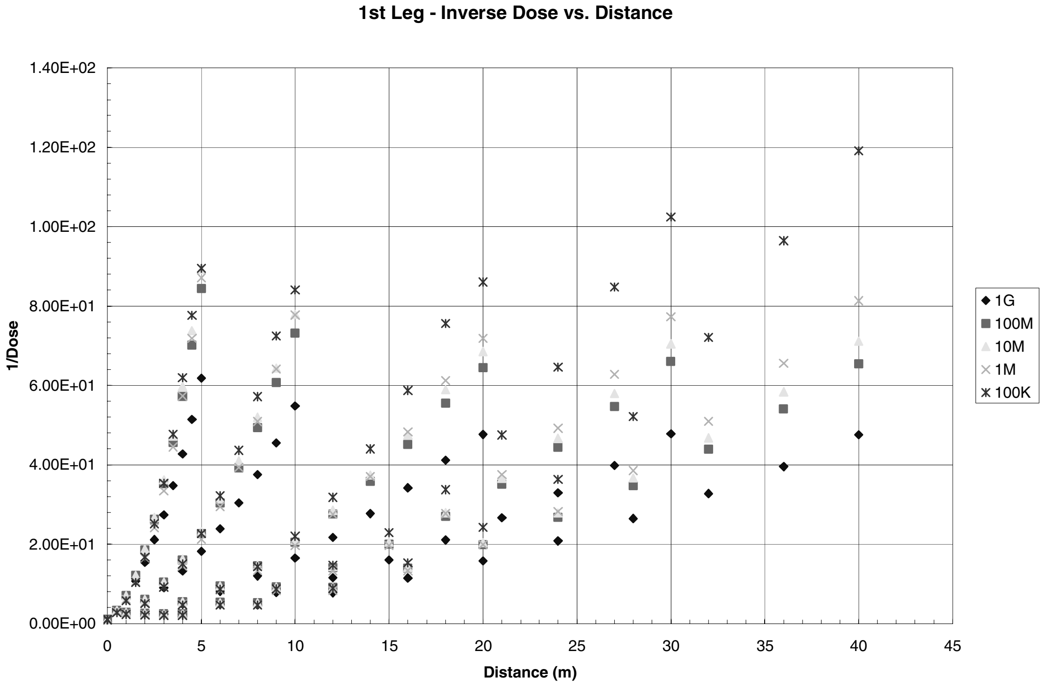

Figure 25 – First leg plot of *A(E,a)*x^n . This plot was used to help visually evaluate the functional form of the first leg transmission.

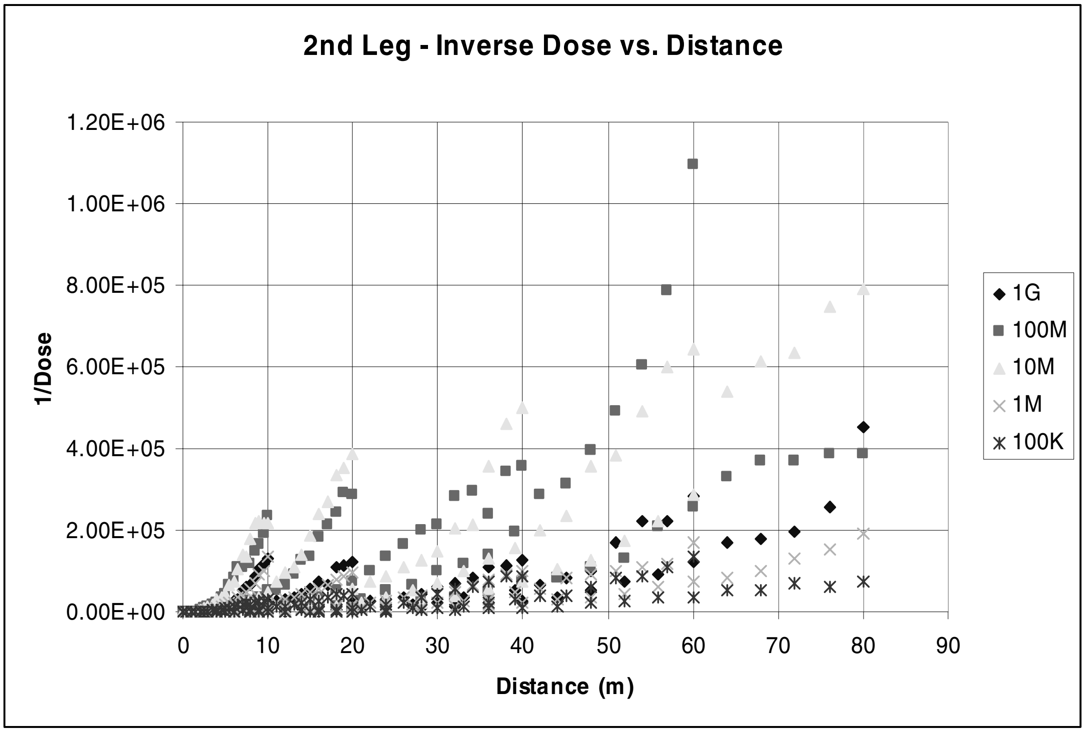

Figure 26 - Second leg plot of $B(E,a)x^n$. This plot was used to help visually evaluate the functional form of the first leg transmission.

Dividing Equation 4 through by different values of x^n give a satisfactory consistency to the values $C(E,a)$ for both the first and second leg. The first leg becomes constant when divided by x^2 and the second leg becomes constant when divided by x^3. Equation 5 is shown in Figure 29. Figure 30 depicts a trend found in the 100 KeV $A(E,a)$ coefficient that an increase in area proportionally increases the value of $A(E,a)$ as the photons travel down the first leg.

$$A(E,a) = \frac{y - 1}{x^2} \tag{5}$$

Equation 6 is shown in Figure 31.

$$B(E,a) = \frac{y - 1}{x^3} \tag{6}$$

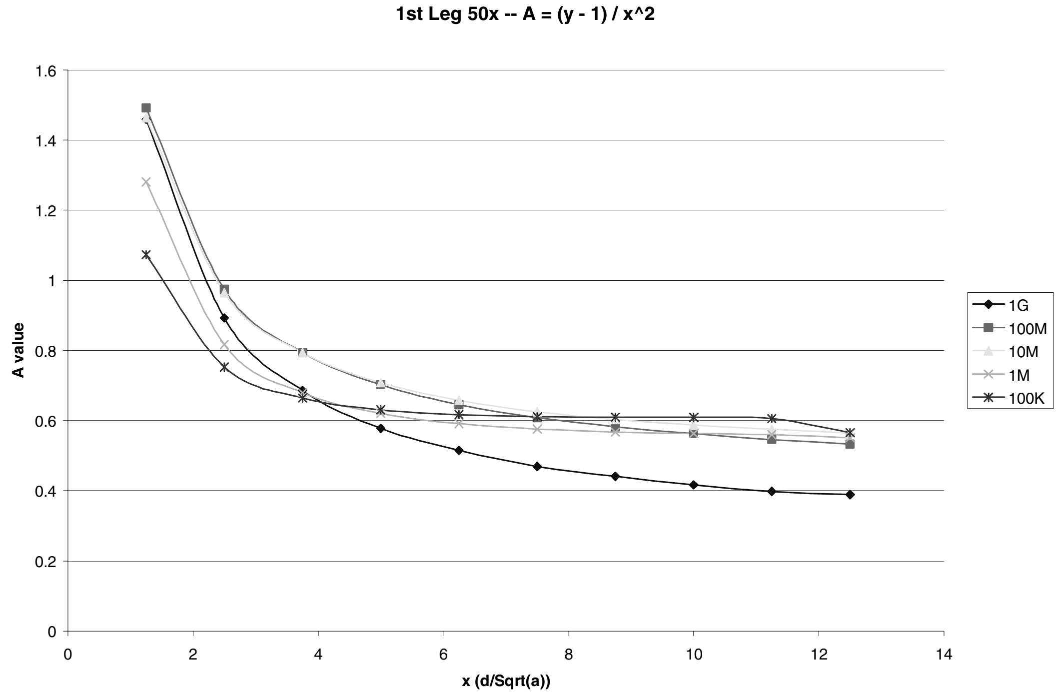

Figure 27 – Plot of *A* vs. *x*, where $A = (y-1)/x^2$. The photon transmission follows a $1/x^2$ curve more closely where A is more constant.

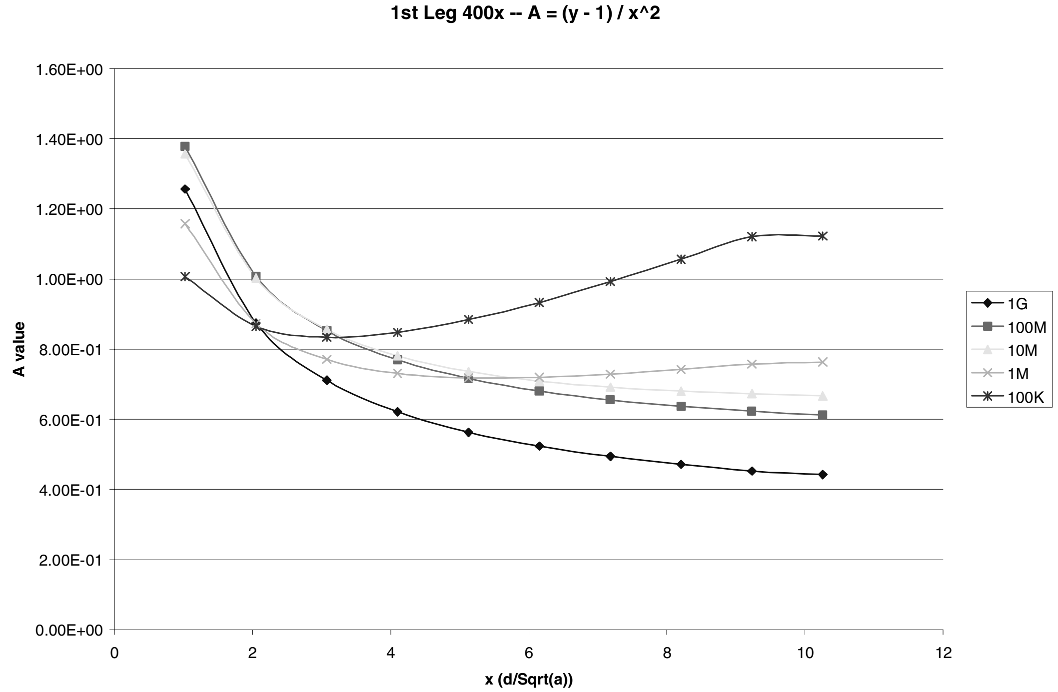

Figure 28 - Plot of *A* vs. *x*, where $A = (y-1)/x^2$, representing the non-constant behavior of the 100 KeV transmission.

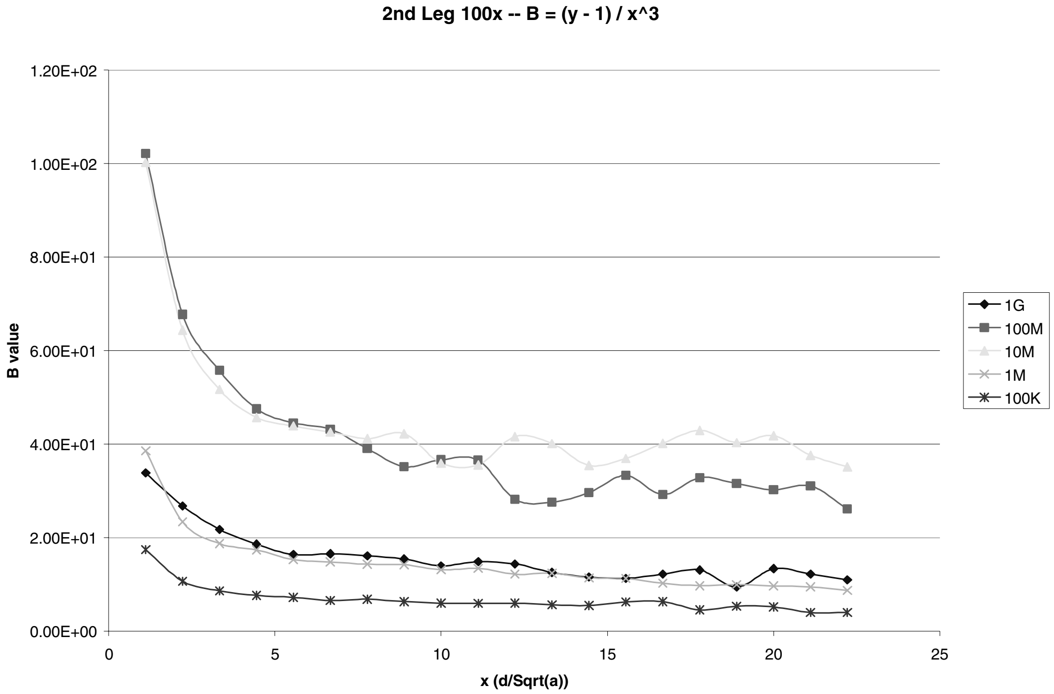

Figure 29 - Plot of B vs. x, where $B = (y-1)/x^3$. The transmission follows a $1/x^3$ curve more closely where B is more constant.

A(E,a) and *B(E,a)* were determined for each data point taken from FLUKA. For each geometry and energy, the mean *A(E,a)* and *B(E,a)* is calculated and tabulated in Table 1. Only the constant region was averaged over. For the first leg, values of $4 < x < 10$ are used. For the second leg, values of $5 < x < 15$ are used. The second leg statistics weaken as x increases (Figure 31), but because the fluctuations in *B(E,a)* do not have a general trend, the effect will add as much to the value of *B(E,a)* as is removed.

Because *A(E,a)* and *B(E,a)* are inversely related the dose, the data points in which low values of *A(E,a)* and *B(E,a)* are used for the fitting curve will result in too high a calculated dose. High values of *A(E,a)* and *B(E,a)* yield too low a calculated dose.

Table 1a – A Coefficient Values

Geometry/Energy	1GeV	100MeV	10MeV	1MeV	100KeV
50x	0.458	0.597	0.617	0.576	0.607
100x	0.503	0.649	0.676	0.642	0.702
200x	0.504	0.654	0.681	0.668	0.784
300x	0.505	0.666	0.694	0.704	0.885
400x	0.510	0.671	0.706	0.737	0.994

Table 1b – B Coefficient Values

Geometry/Energy	1GeV	100MeV	10MeV	1MeV	100KeV
50x	9.499	25.919	25.945	9.794	4.230
100x	15.750	36.798	40.401	14.399	6.790
200x	21.309	63.180	51.359	17.634	10.142
300x	27.506	78.514	62.652	21.280	11.767
400x	32.576	65.810	67.424	22.30	10.421

Equation 3, with appropriate values of *A(E,a)* and *n* substituted, is plotted against the applicable data in Figure 32. Equation 3, with appropriate value of *B(E,a)* and *n* substituted, is plotted against the applicable data in Figure 33.

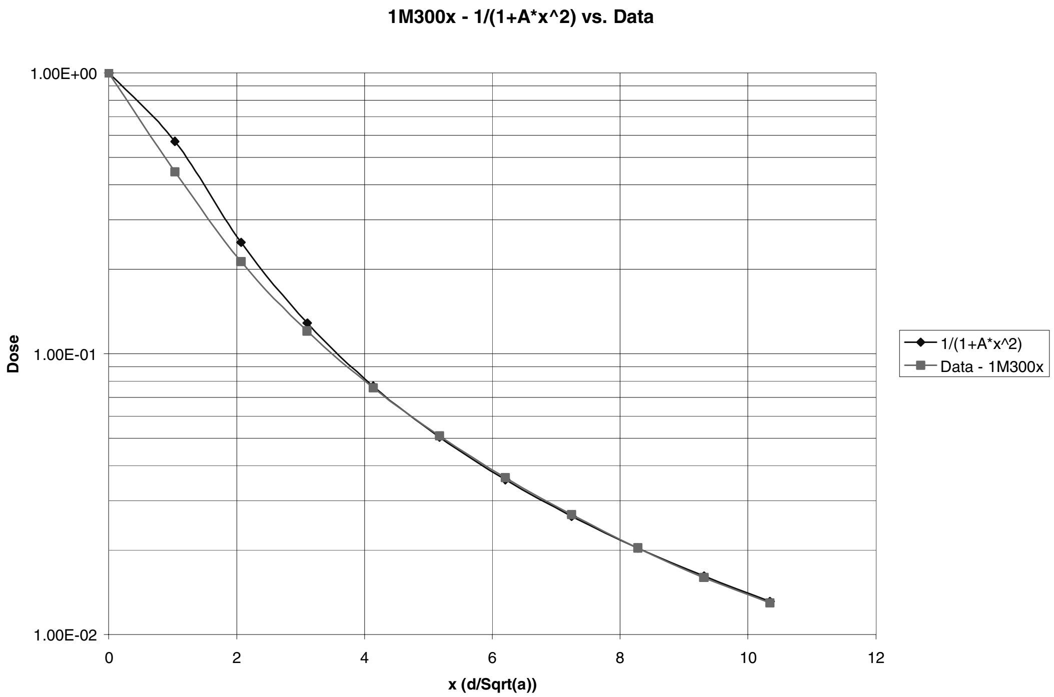

Figure 30 – Fitted curve *1/(1+A*x²)*, where A = 0.704 and the data is from 1 MeV 300 x 300 cm.

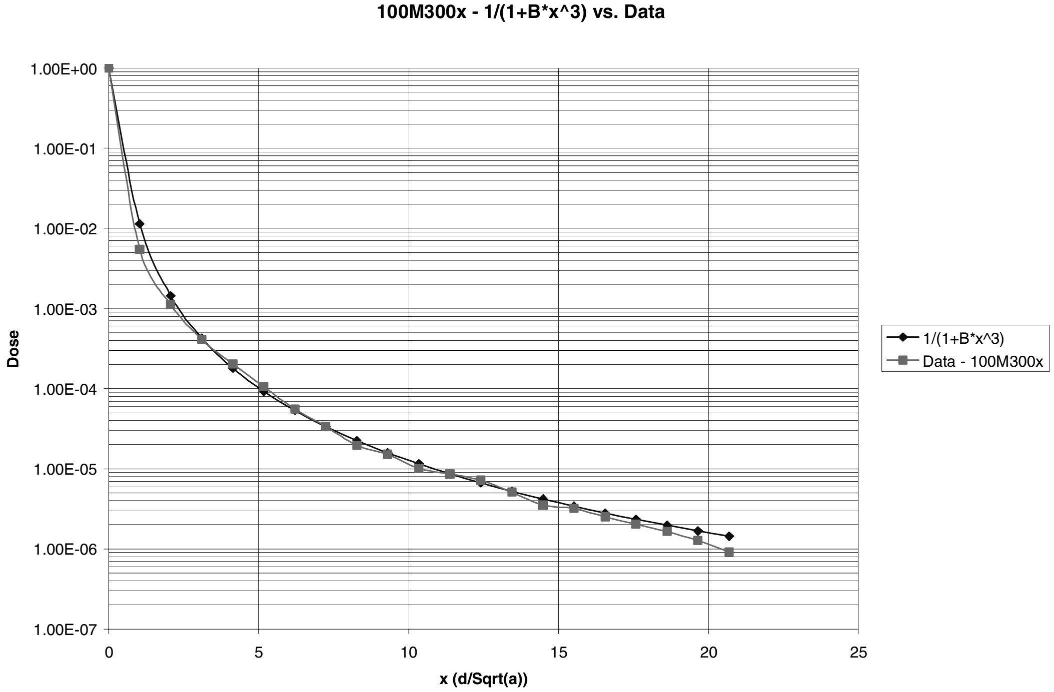

Figure 31 - Fitted curve *1/(1+B*x^3),* where B = 36.80 and the data is from 100 MeV 300 x 300 cm.

To study the functional dependence of *A(E,a)*and *B(E,a)* on energy and geometry, the values of *A(E,a)* and *B(E,a)* are plotted against the geometry and grouped by energy (Figures 34 and 35) and plotted against energy and grouped by geometry (Figures 36 and 37).

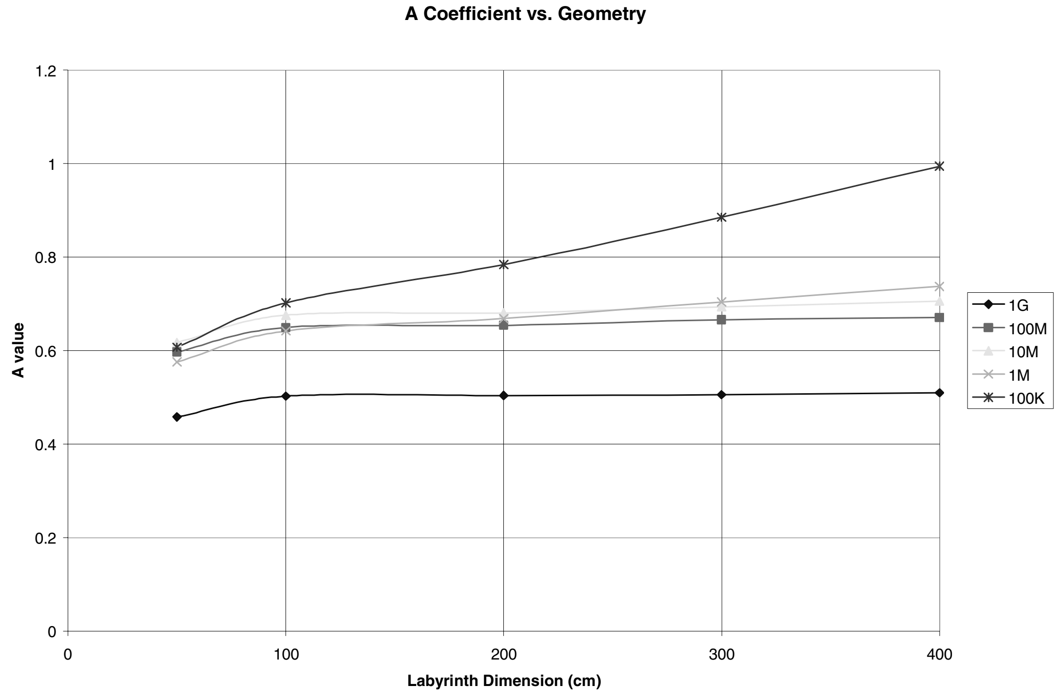

Figure 32 – A coefficient vs. labyrinth geometry. Labyrinth dimension is the length of the side of the square mouth in cm.

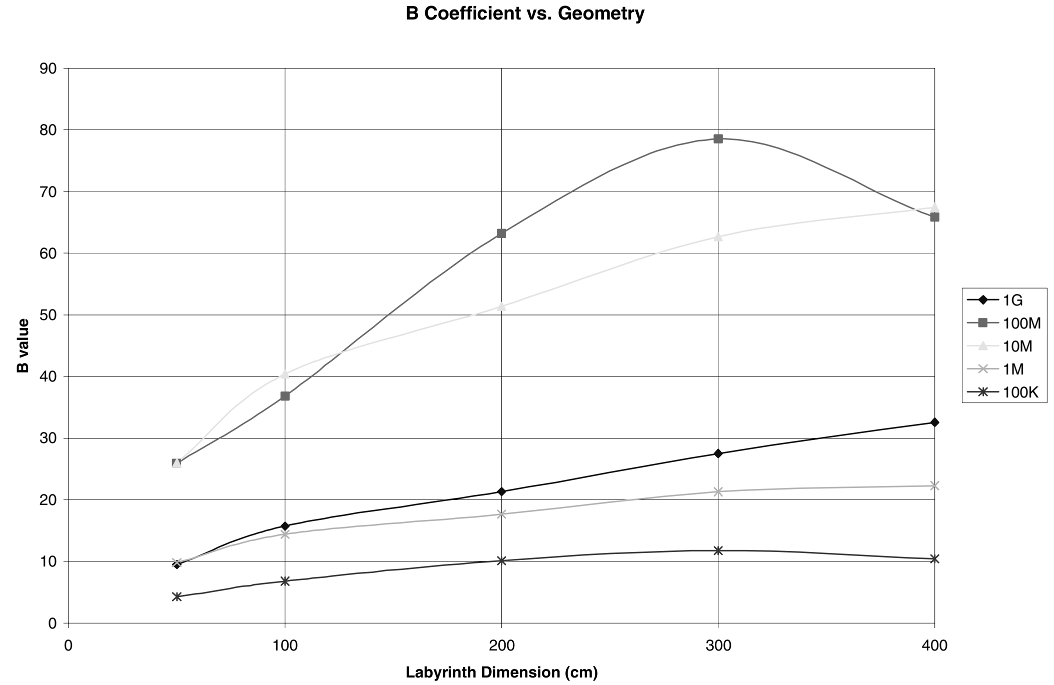

Figure 33 - B coefficient vs. labyrinth geometry. Labyrinth dimension is the length of the side of the square mouth in cm.

In Figures 34 and 35 the energy axis has been scaled logarithmically. A straightforward functional dependence is not readily apparent.

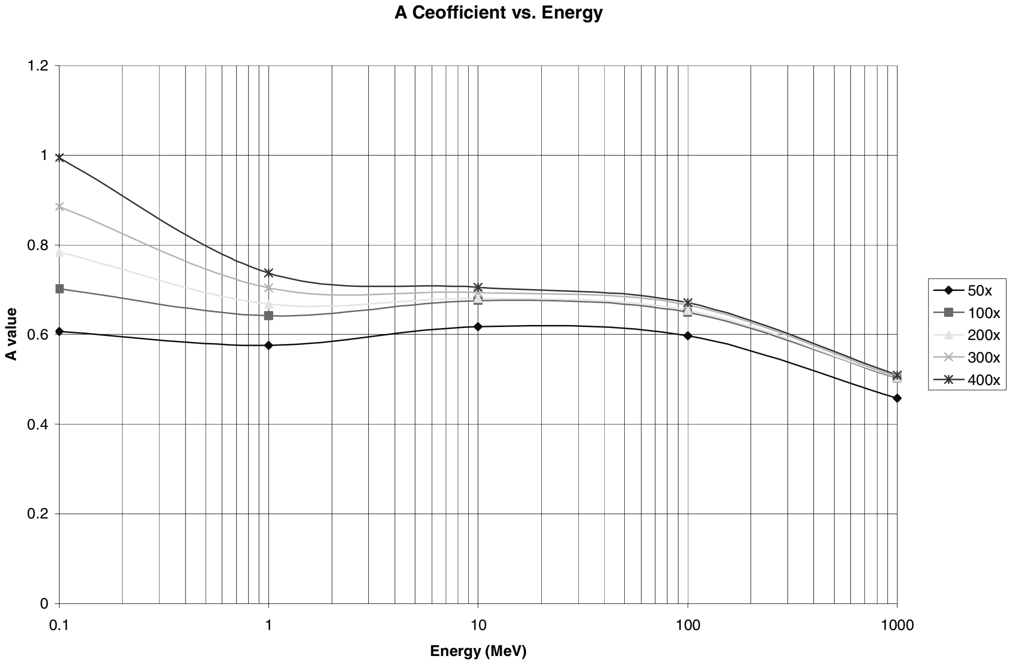

Figure 34 – A coefficient vs. beam energy plotted logarithmically.

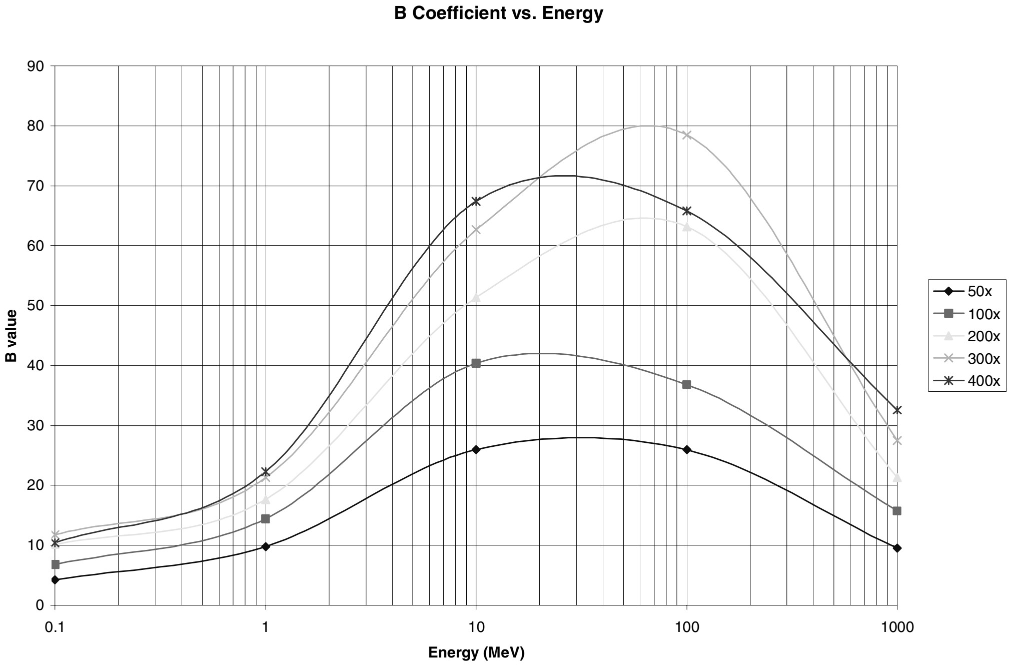

Figure 35 - B coefficient vs. beam energy plotted logarithmically.

Conclusion

Neutrons travel through tunnels and ducts (labyrinths) according to curves that are universally applicable, regardless of labyrinth geometry or particle energy. Photons were believed to follow this manner, but this has been found not to be the case. Photons transmit through labyrinths with a definite functional dependence upon both particle energy and labyrinth geometry. In the first leg of a two-legged labyrinth, photons attenuate according to the function

$$Dose = \frac{1}{1 + A \cdot x^2}$$

In the second leg, photons attenuate according to the function

$$Dose = \frac{1}{1 + B \cdot x^3}$$

in which A and B are functions of energy and labyrinth geometry, and x is a dimensionless unit of d/sqrt(a) where d is the distance from the labyrinth mouth and a is the cross-sectional area. Dose is an attenuation factor. The A and B values have not been analyzed sufficiently to determine their functional dependence upon energy and cross-sectional area, however they have been tabularized which allows for interpolation of the data for use in calculations.

These results were determined by simulating a mono-energetic beam incident upon a two-legged labyrinth with angular spread to cover the mouth. Work was begun on utilizing a real spectrum to determine a functional dependence by placing an iron target at the mouth of the labyrinth, and striking it with an electron beam. However, the techniques used to gather the mono-energetic beam data were not sufficient to effectively gather a complete set of real spectrum data and analyze its functionality.

Appendix A - Prospects

1. Improving Statistics – A technique can be applied where the properties of all the incident particles that reach the end of the first leg of the labyrinth are stored in a single file. This file is then applied to and reused in the second leg multiple times so that a single run can be reproduced and the uncertainty minimized. A third leg or a fourth leg can be added and this technique applied again, allowing statistics to be high enough to study transmission through the second and subsequent legs effectively.
2. Fixed Target Collision – Because the mono-energetic beam case would never be found in an actual accelerator, further work should be applied to the more substantive fixed target collisions. Once a more complete set of data is accrued, similar or more advanced fitting techniques can be applied to gather a functional form of those transmission curves.
3. Off-Axis – What types of transmission can occur in the labyrinth is affected by where the source of the radiation is. Figure 1i shows that a point source off axis loses its primary route of transmission (labeled 1) when it cannot see the back wall of the first leg. It would be interesting to see how this affected the attenuation.
4. Third Leg and Beyond – Part of the prediction that photons will attenuate according to a universal curve was that they would also attenuate according to the same curve for the second leg and all subsequent legs. To determibe if photons follow the same rules as neutrons for the second and subsequent legs is of significant interest.

References

1. Cossairt, J. Donald "Radiation Physics for Personnel and Environmental Protection Revision 5", March 2001, Fermi National Accelerator Laboratory, Chicago IL, pp 5-5
   fnalpubs.fnal.gov/archive/2000/tm/p-TM-1834Chap5.pdf
2. Stevenson, Graham R., Thomas, Ralph H. "Radiological Safety Aspects of the Operation of Proton Accelerators", 1988, International Atomic Energy Agency, Vienna, pp 174
3. Cossairt, J. Donald "Radiation Physics for Personnel and Environmental Protection Revision 5" pp 5-15
4. Stevenson, Graham R., Thomas, Ralph H. "Radiological Safety Aspects of the Operation of Proton Accelerators" pp 176
5. Tesch, K. "Attenuation of the Photon Dose in Labyrinths and Ducts at Accelerators", 2000, Deutsches Electronen-Synchrotron DESY, Hamburg, pp 170